LETTERS
https://doi.org/10.1038/s41567-020-01102-1

nature physics

Check for updates

Non-classical energy squeezing of a macroscopic mechanical oscillator

X. Ma[1,2]✉, J. J. Viennot[1,2,3], S. Kotler[2,4], J. D. Teufel[4] and K. W. Lehnert[1,2]

Optomechanics and electromechanics have made it possible to prepare macroscopic mechanical oscillators in their quantum ground states[1], in quadrature-squeezed states[2] and in entangled states of motion[3]. However, the effectively linear interaction between motion and light or electricity precludes access to the broader class of quantum states of motion, such as cat states or energy-squeezed states. Strong quadratic coupling of motion to light could allow a way around this restriction[4–6]. Although there have been experimental demonstrations of quadratically coupled optomechanical systems[5,7,8], these have not yet accessed non-classical states of motion. Here we create non-classical states by quadratically coupling motion to the energy levels of a Cooper-pair box qubit. Through microwave-frequency drives that change the state of both the oscillator and qubit, we then dissipatively stabilize the oscillator in a state with a large mean phonon number of 43 and sub-Poissonian number fluctuations of approximately 3. In this energy-squeezed state, we observe a striking feature of the quadratic coupling: the recoil of the mechanical oscillator caused by qubit transitions, closely analogous to the vibronic transitions in molecules[9,10].

The ability to access a broad range of quantum states with mechanical oscillators has many applications and is an enduring ambition in the fields of opto- and electromechanics. As mechanical oscillators are linear at the quantum scale, arbitrary quantum control over them requires an extrinsic nonlinearity such as a nonlinear source[11] or detector[12,13]. Alternatively, a mechanical oscillator can be coupled to an ancillary system in a nonlinear manner. For example, opto- and electromechanical systems routinely use the inherently nonlinear radiation-pressure interaction between the motion of a mechanical oscillator and the energy of an ancillary optical or electrical cavity.

However, the radiation-pressure interaction is intrinsically weak; thus, most experiments operate with a large-cavity drive, increasing the coupling strength but yielding a linear interaction between oscillator motion and cavity field. In refs. [5] and [6], the authors propose a solution: by coupling the square of the oscillator motion to the cavity energy, the drive-enhanced coupling remains nonlinear. Despite new theoretical insights[14–17] and rapid experimental progress[7,8,18,19], quadratic coupling schemes for opto- and electromechanics[4] have not yielded non-classical states in mechanical oscillators.

To overcome the weak coupling of electromechanics, in which the zero-point motion of the mechanical oscillator alters the tiny zero-point electrical energy stored in the capacitor of a resonant circuit, we arrange for motion to alter the large electrostatic energy stored in the capacitor of a Cooper-pair box (CPB) qubit by an applied d.c. voltage[20–22] (Fig. 1a,b). At a point of charge degeneracy in the qubit, this arrangement creates a quadratic coupling between the oscillator position and qubit energy (Fig. 1c). We use this quadratic coupling to adiabatically stabilize a mechanical oscillator into an energy-squeezed state with average phonon number of 43 and variance less than 11, yielding a Fano factor of $F = 0.257^{+0.002}_{-0.001}$ far below the classical limit of $F \geq 1$ (ref. [23]). As a consequence of creating this high-energy number-squeezed state, we also observe sidebands in the qubit spectrum that reveal qubit excitation processes that create or annihilate phonons in pairs.

To achieve strong quadratic interaction between the mechanical oscillator and a superconducting qubit, we embed a mechanically compliant elliptical disc into the microwave circuit shown in Fig. 1d,e. The mechanical oscillator is the antisymmetric, second mode of the suspended disc with a resonant frequency $\omega_m \approx 2\pi \times 25\,\mathrm{MHz}$. Underneath the disc, two aluminium electrodes are placed at the antinodes of motion to form two mechanically compliant capacitors. The electrodes are connected through two Josephson junctions in parallel, creating a flux-tunable CPB qubit[24]. A static voltage V_{dc} applied to the disc couples motion to the qubit energy as illustrated by an approximate electromechanical schematic in Fig. 1a (Supplementary Section IB). The symmetry of the capacitor network is broken by the antisymmetric motion of the oscillatory mode, yielding a CPB qubit with a gate voltage $V_g(x)$ proportional to the oscillator's coordinate (Fig. 1b). By applying $V_{dc} = 6\,\mathrm{V}$, we achieve a coupling rate of $g_m \approx 2\pi \times 22\,\mathrm{MHz}$, orders of magnitude larger than the values achieved using radiation-pressure electromechanical coupling[25]. Operating at the charge degeneracy point, the qubit energy is first order insensitive to the oscillator's motion, but the second-order quadratic coupling[14] $2\chi_m \approx (2g_m)^2/(E_J/\hbar) \approx 2\pi \times 0.52\,\mathrm{MHz}$, where E_J is the Josephson energy, is large enough to profoundly affect the qubit and oscillator dynamics.

Although it is expedient[22] to approximate a strong quadratic coupling of motion to a qubit using the dispersive limit of the Jaynes–Cummings Hamiltonian, familiar from circuit quantum electrodynamics (cQED), this approximation fails to fully capture phenomena associated with the large separation in energy scales ($g_m, \omega_m \ll \omega_q$, the qubit frequency). Instead, the oscillator's position behaves as a slow coordinate[26] moving in a potential modified by the state of the qubit[27,28] (see also Supplementary Section IIA),

$$H = \frac{1}{2}\hbar\omega_q\hat{\sigma}_z + \frac{\hat{p}^2}{2m} + \frac{1}{2}k\left(1 + \frac{2\chi_m}{\omega_m}\hat{\sigma}_z\right)\hat{x}^2 \qquad (1)$$

where $\hat{x}$ and $\hat{p}$ are the position and momentum operators of the mechanical oscillator respectively, m and k are the mass and the spring constant, $\hat{\sigma}_z$ is the qubit Pauli operator and $\chi_m = {g_m}^2/(\omega_q - \omega_m) + {g_m}^2/(\omega_q + \omega_m)$ includes the Bloch–Siegert shift[27–29]. The

[1]JILA, National Institute of Standards and Technology and University of Colorado, Boulder, CO, USA. [2]Department of Physics, University of Colorado, Boulder, CO, USA. [3]Université Grenoble Alpes, CNRS, Institut Néel, Grenoble, France. [4]National Institute of Standards and Technology (NIST), Boulder, CO, USA.
✉e-mail: xizheng.ma@colorado.edu

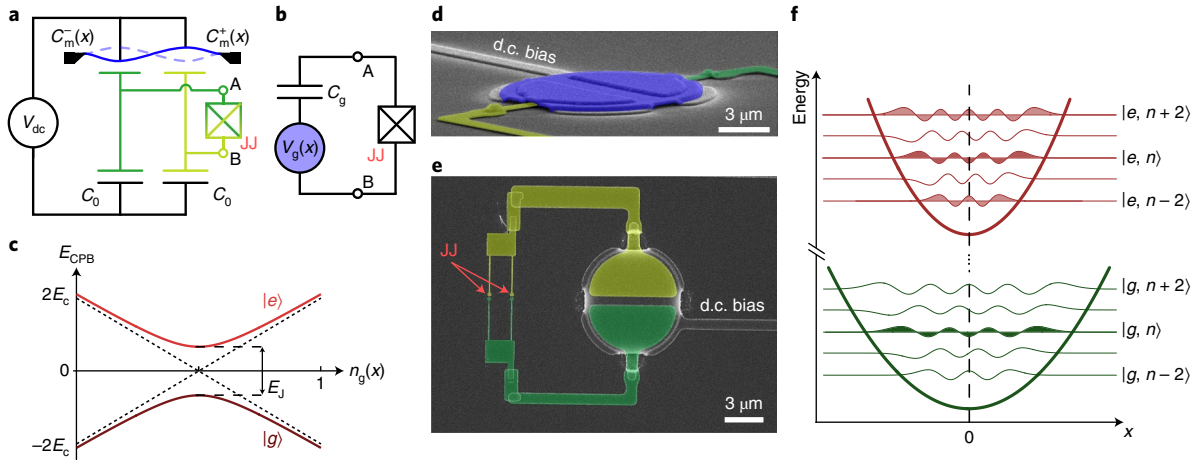

Fig. 1 | Quadratically coupled electromechanics. a, The capacitances of two mechanically compliant capacitors, $C_m^{\pm}(x)$, are modulated with opposite phase by the antisymmetric motion of the mechanical oscillator (blue). An applied voltage V_{dc} converts this modulation of capacitance to a voltage $V_g(x)$ across the open terminals A and B. **b**,**c**, The Thévenin equivalent representation of the circuit seen by the junctions is a CPB qubit (**b**), with a gate capacitance C_g and a mechanical-position-dependent gate charge $n_g(x) = V_g(x)C_g/2e$ that tunes the qubit energy E_{CPB} (**c**). The qubit ground ($|g\rangle$) and excited ($|e\rangle$) states are superpositions of two charge states (dashed lines) of the circuit differing by one Cooper pair, with the average value of the ground- and excited-state energy defined to be zero. These energies are linearly dependent on x with slope $\pm 2\hbar g_m/x_{zp}$, defining g_m as the qubit–mechanics coupling rate. The degeneracy between the charge states at $n_g = 1/2$ (charge degeneracy point) is lifted by the tunnelling of Cooper pairs across the junctions at the rate $E_J/\hbar$. At charge degeneracy, the qubit transition frequency senses the square of mechanical displacement with quadratic coupling strength $(2g_m)^2/(E_J/\hbar)$. **d**, False-coloured scanning electron micrograph (at an angle) of the micromechanical oscillator (blue) suspended above two electrodes (green and yellow) to form mechanically compliant capacitors. The d.c. bias line imposes a voltage on the oscillator plate. **e**, Top view of the device. The two bottom electrodes are shunted by two Josephson junctions (JJ) in parallel to form a superconducting qubit. **f**, A qubit excitation causes a sudden change of the mechanical potential (parabolas) and a non-zero overlap between spatial wavefunctions (lines) of different mechanical states of opposite qubit excitations. Because of symmetry, this process only connects an initial state $|g, n\rangle$ (shaded green) with states of the same mechanical parity $|e, n \pm 2l\rangle$ (shaded red), creating or annihilating phonons in pairs.

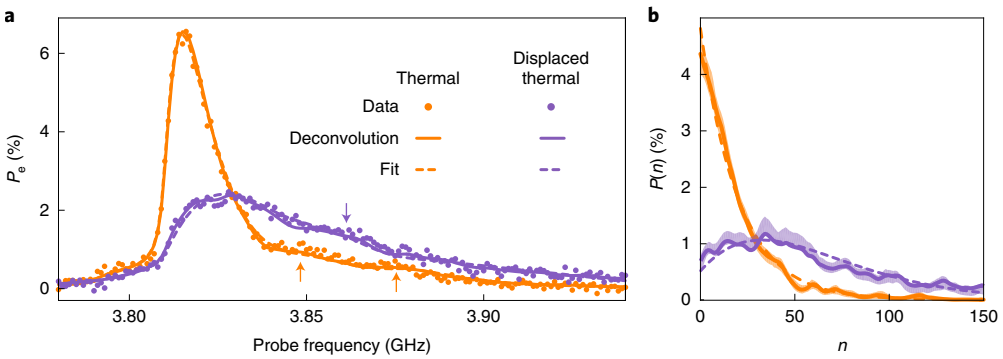

Fig. 2 | Determining the phonon distribution from a qubit spectrum. a, The qubit spectrum is measured when the mechanical oscillator is in a thermal state or a displaced thermal state. Although individual sideband peaks are not resolvable because of the broad phonon distribution, we can still observe features associated with them at the positions highlighted by the vertical arrows. We perform a least-squares fit on the thermal-state qubit spectrum (solid orange line) using equation (2), assuming a thermal distribution (dashed orange line) with only two free parameters: $n_{th} = 17.7$ and the bare qubit frequency (Supplementary Section IIID). Holding these parameters fixed and assuming a displaced-thermal-state distribution, we also fit the purple data to find the only free parameter $n_{disp} = 43.3$. **b**, Alternatively, we can extract the phonon distributions without assuming a particular form using a deconvolution procedure (solid lines) and find their 90% confidence intervals (shaded areas) using non-parametric bootstrapping. For comparison, we also plot the associated qubit spectra (solid lines) in **a**, and the fitted phonon distributions (dashed lines) in **b**. The presented data are representative of other displaced thermal states we measure, where we confirm that the extracted n_{disp} scales linearly with the power of the displacement drive (Supplementary Section V).

slow mechanical oscillator thus experiences a sudden compression of its effective spring constant $k(\hat{\sigma}_z) = k(1 + 2\chi_m\hat{\sigma}_z/\omega_m)$ when the qubit changes state, which simultaneously alters the mechanical frequency $\omega_m(\hat{\sigma}_z) = \sqrt{k(\hat{\sigma}_z)/m}$ and the mechanical impedance $Z_m(\hat{\sigma}_z) = \sqrt{k(\hat{\sigma}_z)m}$. Because the impedance determines the spatial scale of the qubit-state-dependent mechanical wavefunctions, wavefunctions that differ by even phonon numbers and with opposite qubit excitation are not orthogonal (Fig. 1f). Consequently, the qubit spectrum will exhibit sideband features associated with the pair-wise creation and destruction of phonons. Although they are analogous to the sideband transitions in cQED systems[30,31] where the oscillator and qubit frequencies are comparable, the small ω_m

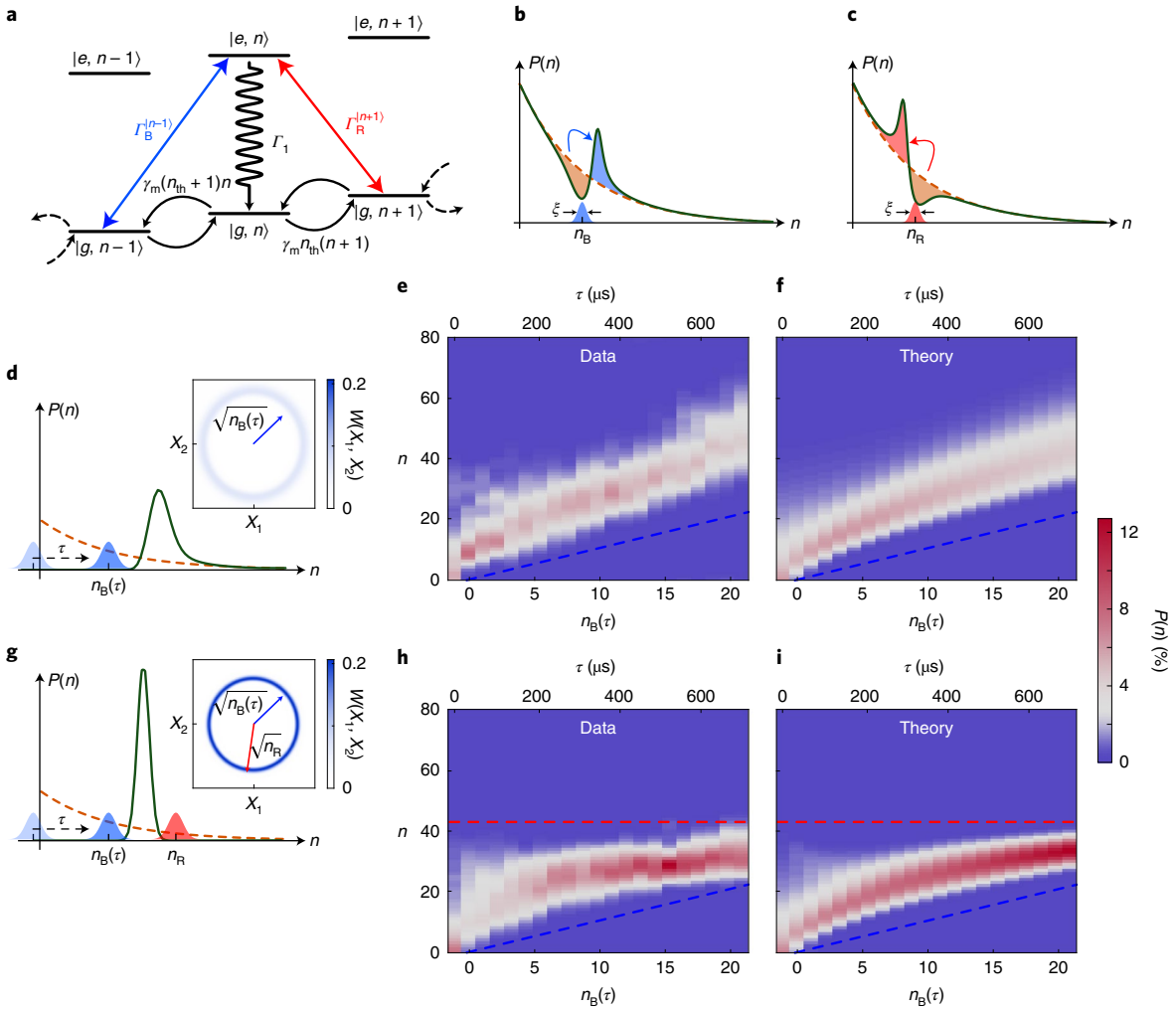

Fig. 3 | Dissipative energy squeezing. a, When the blue sideband transition $|g, n-1\rangle \leftrightarrow |e, n\rangle$ is driven continuously at rate $\Gamma_B^{|n-1\rangle}$ and the qubit decay rate is the dominant relaxation process ($\gamma_m \ll \Gamma_1$), the combination of the two results in the addition of one phonon in the mechanical oscillator at rate $\Gamma_B^{|n+1\rangle}$. ($\Gamma_1 > \Gamma_B^{|n-1\rangle}$ for this work.) Similarly, a red sideband drive removes one phonon at rate $\Gamma_R^{|n+1\rangle}$. **b**,**c**, The sideband drives are phonon-number sensitive, addressing a section of the phonon population centred at n_B or n_R with $\xi \approx 7.1$ phonons. A blue (**b**) or red (**c**) sideband drive applied on an initial thermal state (dashed orange line) creates a distortion in the phonon population (solid green line) at timescale $n_B/\Gamma_B^{|n_B\rangle}$ or $n_R/\Gamma_R^{|n_R\rangle}$. **d**, Alternatively, adiabatically increasing the blue sideband drive frequency (chirping) should empty all phonon population below the final value of n_B. Inset: the resulting state's Wigner function $W(X_1, X_2)$ is a narrow ring around the (X_1, X_2) quadrature space origin with inner radius approximately given by $\sqrt{n_B}$. **e**, Chirping the sideband drive to a final position of $n_B(\tau)$ (bottom axis) by stopping the chirp at time τ (top axis), we measure the qubit spectrum (Supplementary Fig. 11) and extract the phonon distribution (colour scale versus y axis) using deconvolution. At any time, the population is empty below the line $n = n_B(\tau)$ (dashed blue). **f**, Using a master equation calculation, we find the expected phonon distribution for the chirping protocol used in **e** (Supplementary Section VII). **g**, When the blue sideband drive is chirped toward a static red sideband drive centred at n_R, the phonon population should be trapped in between, and squeezed in number space. Inset: the Wigner function of the resulting energy-squeezed state is non-Gaussian and radially symmetric about the quadrature space origin, quite distinct from a quadrature-squeezed state. **h**,**i**, As in **e** and **f**, we compare the measured (**h**) and the expected (**i**) phonon distribution for this energy-squeezing protocol with $n_R = 44$ (dashed red line).

($\ll \omega_q$) means that these electromechanical sidebands not only appear close to the qubit frequency, but also are likely to be excited by a change in the qubit state. Indeed, a qubit transition is likely to alter the phonon number n when the qubit-induced change in mean mechanical energy $\delta k\langle \hat{x}^2 \rangle/2 = 2\hbar\chi_m n$ is larger than the energy of two phonons $2\hbar\omega_m$. Thus, the condition $\chi_m n/\omega_m \gtrsim 1$ signifies the entry into a new regime where phonon-altering qubit transitions become dominant over phonon-preserving transitions.

Nevertheless, similarly to cQED experiments[32], the qubit-state-dependent mechanical frequency $\omega_m(\hat{\sigma}_z)$ leads to a phonon-number-dependent Stark shift on the qubit resonance. We use this shift in qubit frequency to determine the phonon distribution of the mechanical oscillator with a precision given by the phonon-number sensitivity[22] $\xi = \Gamma_2^*/2\chi_m \approx 7.1$ phonons, where Γ_2^* is the qubit decoherence rate. The probability of exciting the qubit as a function of the frequency of a weak qubit-drive tone (qubit spectroscopy) is given by

$$P_e(\omega) = \sum_n P(n) \times P_e^{|n\rangle}(\omega) \qquad (2)$$

—a convolution between the phonon distribution $P(n)$ and the qubit spectrum with exactly n phonons in the mechanical oscillator, $P_e^{|n\rangle}(\omega)$. In contrast to ref. [22], where $P_e^{|n\rangle}(\omega)$ are treated simply as

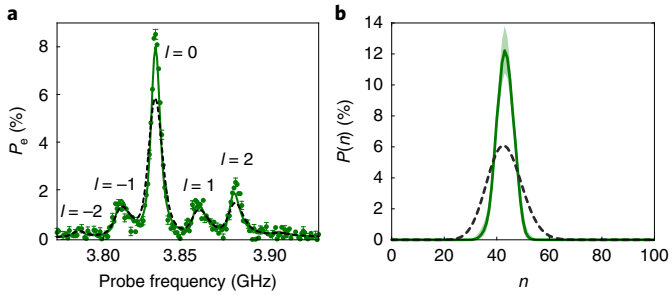

Fig. 4 | Dissipatively stabilized sub-Poissonian state. a, The qubit spectrum (circles) is measured after an optimized energy-squeezing protocol. The s.e.m. is extracted individually for each frequency point (Supplementary Section IX), and plotted as error bars for every fourth point. **b**, The phonon distribution (solid green line) with its 90% confidence interval (shaded green area) is extracted from a deconvolution procedure, and is found to be sub-Poissonian and characterized by $F = 0.257 < 1$. For reference, the phonon distribution and the expected qubit spectrum are plotted for a coherent state (Poissonian, dashed black line). In the qubit spectrum (**a**), the sub-Poissonian nature of the mechanical state is evident in the narrower lineshape. The peaks visible are separated by ω_m, and correspond to transitions $|g, n\rangle \rightarrow |e, n+l\rangle$.

Stark-shifted Lorentzians, we employ a deconvolution[33] procedure that accounts for the sideband transitions in these qubit spectra. This more accurate procedure is necessary because we endeavour to create states with large average phonon number and small distributions. However, its implementation requires that we accurately determine $P_e^{|n\rangle}(\omega)$. As explained in Supplementary Section III, this determination is experimentally achieved by setting $V_{dc} = 0$ V and simulating the effect of motion with a classical a.c. voltage that modulates the gate charge at ω_m.

To validate the deconvolution procedure, we demonstrate it on thermal and displaced thermal states in the mechanical oscillator as shown in Fig. 2. We measure the qubit spectrum and compare the phonon distribution extracted from the deconvolution procedure with that expected for a thermal or displaced thermal state. The good agreement between the phonon distributions as well as the associated qubit spectra substantiates the deconvolution procedure. In the dressed qubit spectra (Fig. 2a), individual sideband peaks cannot be resolved because these features are smeared by the large phonon-number variance. Nevertheless, features associated with those sidebands can be observed at the positions highlighted by the arrows.

With the ability to extract the phonon distribution, we now use sideband transitions (Fig. 3a) to reduce the variance in phonon number. We squeeze the phonon population in Fock space (energy squeezing) by trapping it in between phonon-creating (blue) and phonon-annihilating (red) sideband transitions. Continuously driving these sideband transitions alters the dissipative environment of the mechanical oscillator and changes the steady-state phonon distribution, as evident from the simplified[28] system dynamics of Fig. 3a (see also Supplementary Section VIIA). Because $\Gamma_2^\star$ is much faster than all of the transition rates in these experiments, the final mechanical state contains no quantum coherence, and is fully described by the diagonal elements of its density matrix. Similarly to ref. [22], we adopt the technique[30] of driving a.c.-dither sidebands to access single-phonon sideband transitions (Supplementary Section VI). In contrast to that in conventional linear optomechanics[1], these transitions are crucially different in their phonon-number sensitivity[22]. Leveraging this feature, we address only a section of the phonon population with a characteristic width ξ and displace it in number space (Fig. 3b,c). By slowly increasing the blue sideband drive frequency ω_B (chirping), we adiabatically move the centre of the addressed transitions n_B up in phonon space (Fig. 3d). In Fig. 3e, we show the effect of the chirp. Extracting the phonon population through reconstruction, we observe that the phonon population is emptied below n_B and pushed to a higher occupation. In Fig. 3g–i, we squeeze the phonon population by turning on a red sideband drive centred on the transition $|g, n_R\rangle \leftrightarrow |e, n_R - 1\rangle$, with n_R close to but greater than the maximum value of n_B. A Fock state $|n\rangle$ will be cooled to a lower occupancy when the blue sideband transition rate is slower than the red sideband transition rate $\Gamma_B^{|n\rangle} < \Gamma_R^{|n\rangle}$, and vice versa. Thus, under conditions $\Gamma_B^{|n_B\rangle} > \Gamma_R^{|n_B\rangle}$ and $\Gamma_B^{|n_R\rangle} < \Gamma_R^{|n_R\rangle}$, a state that starts with $n_R > n > n_B$ cannot escape the bounds of the two sideband drives. Additionally, states with $n > n_R$ are eventually trapped between n_R and n_B by a combination of thermal equilibration and the action of the red sideband drive[22]. Requiring neither number resolution nor coherent manipulation, this energy-squeezing technique can be easily implemented in other cQED experiments.

In Fig. 4, we use energy squeezing to prepare the mechanical oscillator in a non-classical state. After optimizing the relative power and position of the two sideband drives, we squeeze the phonon population at mean phonon number $\langle n\rangle = 43$ and prepare it in a sub-Poissonian state. We characterize the non-classical nature of this state with $F = \mathrm{var}(n)/\langle n\rangle$. For a Poisson-distributed state $F = 1$, and for a Fock state $F = 0$. When $F < 1$, the phonon distribution is non-classical[23], energy squeezed and Fock-like. Extracting the phonon distribution through reconstruction, we find $F = 0.257^{+0.002}_{-0.001}$, where the bound is determined by the uncertainty in the bare qubit frequency. To quantify the confidence in the extracted Fano factor $F_{extract}$, we perform repeated reconstruction procedures on simulated experiments that have specified phonon distributions with $\langle n\rangle = 43$ and Fano factors F_{true}, as described in Supplementary Section IX. For a given range of $F_{extract}$, we can bound F_{true}. Specifically, for $F_{extract}$ within the interval [0.255, 0.265] we find $F_{true} \leq 0.28$ with 95% confidence, and $F_{true} \leq 0.30$ with 99% confidence. This Fano factor can be related to a negativity in the Wigner function under the assumption of a Gaussian number distribution[34] (Supplementary Section X). We have thus demonstrated our ability to prepare a type of highly non-classical mechanical state with high average energy but small fluctuations, quite distinct from quadrature-squeezed states. We choose to squeeze around $\langle n\rangle = 43$, where the spurious cooling effect (Supplementary Section VIII) is small and the phonon population dynamics are more intuitive. However, because this method of energy squeezing creates states with a minimum width of $\xi \approx 7.1$ phonons independent of $\langle n\rangle$, it is conceivable to achieve a smaller F by squeezing at higher $\langle n\rangle$.

In creating this energy-squeezed state, we can now resolve the sideband transitions that were obscured by the broad phonon distribution associated with the large thermal occupation in Fig. 2a. The centre peak in the qubit spectroscopy ($l = 0$ peak in Fig. 4a) corresponds to the qubit transition that conserves phonon number, whereas the satellite peaks at $\pm 2\omega_m$ ($l = \pm 2$) are mostly associated with qubit transitions that create and annihilate pairs of phonons when the mechanical spring suddenly stiffens. Because charge noise creates a small random bias away from degeneracy, we also observe peaks at $\pm\omega_m$ associated with single-phonon sideband transitions (Supplementary Section IIC). In contrast to the sidebands observed in ref. [21] at $\langle n\rangle \sim 10^4$ phonons, these peaks are easily resolved at the relatively small phonon number $\langle n\rangle = 43$ because χ_m/ω_m is much larger. Consequently, they can substantially alter the oscillator's phonon distribution.

The prominence of these sideband peaks also signifies the entry into a regime where the qubit's spontaneous decay can detectably alter the phonon distribution[28] (Supplementary Section VIIA). In Fig. 4a, we measure the probability of exciting the qubit when driving at a particular frequency, but each peak must also correspond

to a qubit decay process, driven by the quantum noise in the environment. From the ratio of the area underneath the $l=0$ peak to the total area under all the peaks, we estimate that a qubit decaying from an initial state of $|e,43\rangle$ will only preserve the phonon number with 63% probability. This probability will further diminish if χ_m is increased to better resolve individual phonon numbers.

Online content

Any methods, additional references, Nature Research reporting summaries, source data, extended data, supplementary information, acknowledgements, peer review information; details of author contributions and competing interests; and statements of data and code availability are available at https://doi.org/10.1038/s41567-020-01102-1.

Received: 6 May 2020; Accepted: 22 October 2020;
Published online: 4 January 2021

References

1. Teufel, J. D. et al. Sideband cooling of micromechanical motion to the quantum ground state. *Nature* **475**, 359–363 (2011).
2. Wollman, E. E. et al. Quantum squeezing of motion in a mechanical resonator. *Science* **349**, 952–955 (2015).
3. Palomaki, T. A., Teufel, J. D., Simmonds, R. W. & Lehnert, K. W. Entangling mechanical motion with microwave fields. *Science* **342**, 710–713 (2013).
4. Braginsky, V. B., Vorontsov, Y. I. & Thorne, K. S. Quantum nondemolition measurements. *Science* **209**, 547–557 (1980).
5. Thompson, J. D. et al. Strong dispersive coupling of a high-finesse cavity to a micromechanical membrane. *Nature* **452**, 72–75 (2008).
6. Jayich, A. M. et al. Dispersive optomechanics: a membrane inside a cavity. *New J. Phys.* **10**, 095008 (2008).
7. Brawley, G. A. et al. Nonlinear optomechanical measurement of mechanical motion. *Nat. Commun.* **7**, 10988 (2016).
8. Leijssen, R., La Gala, G. R., Freisem, L., Muhonen, J. T. & Verhagen, E. Nonlinear cavity optomechanics with nanomechanical thermal fluctuations. *Nat. Commun.* **8**, ncomms16024 (2017).
9. Franck, J. & Dymond, E. G. Elementary processes of photochemical reactions. *Trans. Faraday Soc.* **21**, 536–542 (1926).
10. Condon, E. A theory of intensity distribution in band systems. *Phys. Rev.* **28**, 1182–1201 (1926).
11. Reed, A. P. et al. Faithful conversion of propagating quantum information to mechanical motion. *Nat. Phys.* **13**, 1163–1167 (2017).
12. Riedinger, R. et al. Non-classical correlations between single photons and phonons from a mechanical oscillator. *Nature* **530**, 313–316 (2016).
13. Lecocq, F., Teufel, J. D., Aumentado, J. & Simmonds, R. W. Resolving the vacuum fluctuations of an optomechanical system using an artificial atom. *Nat. Phys.* **11**, 635–639 (2015).
14. Miao, H., Danilishin, S., Corbitt, T. & Chen, Y. Standard quantum limit for probing mechanical energy quantization. *Phys. Rev. Lett.* **103**, 100402 (2009).
15. Jacobs, K., Tian, L. & Finn, J. Engineering superposition states and tailored probes for nanoresonators via open-loop control. *Phys. Rev. Lett.* **102**, 057208 (2009).
16. Dellantonio, L., Kyriienko, O., Marquardt, F. & Sørensen, A. S. Quantum nondemolition measurement of mechanical motion quanta. *Nat. Commun.* **9**, 3621 (2018).
17. Hauer, B. D., Metelmann, A. & Davis, J. P. Phonon quantum nondemolition measurements in nonlinearly coupled optomechanical cavities. *Phys. Rev. A* **98**, 043804 (2018).
18. Doolin, C. et al. Nonlinear optomechanics in the stationary regime. *Phys. Rev. A* **89**, 053838 (2014).
19. Paraïso, T. K. et al. Position-squared coupling in a tunable photonic crystal optomechanical cavity. *Phys. Rev. X* **5**, 041024 (2015).
20. LaHaye, M. D., Suh, J., Echternach, P. M., Schwab, K. C. & Roukes, M. L. Nanomechanical measurements of a superconducting qubit. *Nature* **459**, 960–964 (2009).
21. Pirkkalainen, J.-M. et al. Hybrid circuit cavity quantum electrodynamics with a micromechanical resonator. *Nature* **494**, 211–215 (2013).
22. Viennot, J. J., Ma, X. & Lehnert, K. W. Phonon-number-sensitive electromechanics. *Phys. Rev. Lett.* **121**, 183601 (2018).
23. Short, R. & Mandel, L. Observation of sub-Poissonian photon statistics. *Phys. Rev. Lett.* **51**, 384–387 (1983).
24. Makhlin, Y., Schön, G. & Shnirman, A. Quantum-state engineering with Josephson-junction devices. *Rev. Mod. Phys.* **73**, 357–400 (2001).
25. Teufel, J. D. et al. Circuit cavity electromechanics in the strong-coupling regime. *Nature* **471**, 204–208 (2011).
26. Ashhab, S. & Nori, F. Qubit-oscillator systems in the ultrastrong-coupling regime and their potential for preparing nonclassical states. *Phys. Rev. A* **81**, 042311 (2010).
27. Zueco, D., Reuther, G. M., Kohler, S. & Hänggi, P. Qubit-oscillator dynamics in the dispersive regime: analytical theory beyond the rotating-wave approximation. *Phys. Rev. A* **80**, 033846 (2009).
28. Beaudoin, F., Gambetta, J. M. & Blais, A. Dissipation and ultrastrong coupling in circuit QED. *Phys. Rev. A* **84**, 043832 (2011).
29. Bloch, F. & Siegert, A. Magnetic resonance for nonrotating fields. *Phys. Rev.* **57**, 522–527 (1940).
30. Blais, A. et al. Quantum-information processing with circuit quantum electrodynamics. *Phys. Rev. A* **75**, 032329 (2007).
31. Wallraff, A. et al. Sideband transitions and two-tone spectroscopy of a superconducting qubit strongly coupled to an on-chip cavity. *Phys. Rev. Lett.* **99**, 050501 (2007).
32. Schuster, D. I. et al. Resolving photon number states in a superconducting circuit. *Nature* **445**, 515–518 (2007).
33. Richardson, W. H. Bayesian-based iterative method of image restoration. *J. Opt. Soc. Am.* **62**, 55–59 (1972).
34. Lörch, N., Qian, J., Clerk, A., Marquardt, F. & Hammerer, K. Laser theory for optomechanics: limit cycles in the quantum regime. *Phys. Rev. X* **4**, 011015 (2014).

Publisher's note Springer Nature remains neutral with regard to jurisdictional claims in published maps and institutional affiliations.

© The Author(s), under exclusive licence to Springer Nature Limited 2021

Data availability

Source data are provided with this paper. All other data that support the plots within this paper and other findings of this study are available from the corresponding author upon reasonable request.

Code availability

The codes that support the plots within this paper and other findings of this study are available from the corresponding author upon reasonable request.

Acknowledgements

We thank D. Palken, L. Sletten, R. Delaney, F. Beaudoin and L. Tian for fruitful discussions. We gratefully acknowledge R. Simmonds and F. Lecocq for their help with the fabrication of the device. We thank M. Malnou and D. Palken for providing us with a Josephson parametric amplifier. We acknowledge funding from National Science Foundation (NSF) under grant no. PHY-1734006. J.J.V. acknowledges financial support from the European Union's H2020 programme under Marie Skłodowska-Curie grant no. 841618

Author contributions

X.M., J.J.V. and K.W.L. conceived and designed the experiment, X.M. and J.J.V. fabricated the device and performed the experiment, X.M., S.K., J.J.V. and K.W.L. derived the theory and analysed the data and X.M., K.W.L. and J.D.T. prepared the manuscript. All authors provided suggestions for the experiment, discussed the results and contributed to the manuscript.

Competing interests

The authors declare no competing interests.

Additional information

Supplementary information is available for this paper at https://doi.org/10.1038/s41567-020-01102-1.

Correspondence and requests for materials should be addressed to X.M.

Peer review information *Nature Physics* thanks Adrian Bachtold, Mario Gely, Gary Steele and the other, anonymous, reviewer(s) for their contribution to the peer review of this work.

Reprints and permissions information is available at www.nature.com/reprints.